lubricants

MDPI

Article

Tribological and Oxidation-Induced Degradation of Engine Materials Fueled with Bio-Hydrogenated Diesel–Biodiesel Blends

Sathaporn Chuepeng [1], Atthaphon Maneedaeng [2], Niti Klinkaew [3], Anupap Pumpuang [3], Tanongsak Sukkasem [2] and Ekarong Sukjit [4,*]

[1] Department of Mechanical Engineering, Faculty of Engineering at Sriracha, Kasetsart University, 199 Sukhumvit Road, Chonburi 20230, Thailand; schuepeng@eng.src.ku.ac.th
[2] School of Chemical Engineering, Institute of Engineering, Suranaree University of Technology, Nakhon Ratchasima 30000, Thailand; atthaphon@sut.ac.th (A.M.); garmotanongsak@gmail.com (T.S.)
[3] Institute of Research and Development, Suranaree University of Technology, Nakhon Ratchasima 30000, Thailand; niti_nick@hotmail.com (N.K.); anupappumpuang@gmail.com (A.P.)
[4] School of Mechanical Engineering, Institute of Engineering, Suranaree University of Technology, Nakhon Ratchasima 30000, Thailand
* Correspondence: ekarong@sut.ac.th

Abstract

Although bio-hydrogenated diesel (BHD) offers drop-in compatibility and high oxidative stability, its poor lubricity remains a critical barrier to long-term engine deployment. Previous studies have primarily relied on short-term tribological assessments, leaving insufficient empirical data on sustained wear behavior under realistic conditions. This study addresses that gap through a 200 h durability evaluation of BHD–biodiesel blends in a single-cylinder diesel engine under constant load conditions per Thai Industrial Standard TIS 2618-2557. Five fuels, namely diesel, pure BHD, BHD90, BHD70, and pure biodiesel, were tested to identify the critical biodiesel threshold for optimal tribological and oxidative performance. BHD90 (90% BHD + 10% biodiesel) emerged as the optimal formulation, delivering the lowest torque reduction (11.2%) and minimal iron wear particles (101 ppm), while preserving oxidation stability. Biodiesel concentrations exceeding 10% induced accelerated lubricant oxidation through hygroscopic effects, negating the lubricity benefits. Fourier-transform infrared spectroscopy (FTIR) analysis of piston carbon deposits further revealed that higher biodiesel blends produced more oxygenated compounds, whereas pure BHD and diesel generated predominantly aliphatic hydrocarbons. These findings establish a mechanistic relationship between fuel composition, oxidation, and wear under endurance conditions, providing a practical guideline for renewable diesel formulation that balances lubrication performance, oxidation control, and long-term engine durability.

Keywords: bio-hydrogenated diesel; biodiesel; engine wear; lubricant contamination; engine durability test

Check for updates

Received: 14 March 2026
Revised: 12 April 2026
Accepted: 17 April 2026
Published: 20 April 2026

Copyright: © 2026 by the authors. Licensee MDPI, Basel, Switzerland. This article is an open access article distributed under the terms and conditions of the Creative Commons Attribution (CC BY) license.

1. Introduction

In recent years, green diesel (bio-hydrogenated diesel or BHD) has garnered significant attention in the renewable fuel sector due to its biodegradability, paraffinic hydrocarbon composition, and sustainable feedstock sources, offering numerous advantages over traditional petroleum-derived diesel [1]. BHD is produced through the hydrogenation of

triglycerides from renewable sources such as palm oil, which is Thailand's primary vegetable oil feedstock, resulting in a high-quality fuel with an excellent cetane number and cold flow properties [2]. Despite these benefits, BHD suffers from inferior lubricity properties attributed to the non-polar nature of its paraffinic components and lower viscosity, resulting in compromised metal-to-metal interactions in fuel delivery systems [3]. This limitation poses a substantial challenge for engine durability during long-term operation, potentially accelerating component wear in high-pressure common rail fuel injection systems and other precision engine parts that rely on fuel lubrication [4].

Biodiesel, another well-established renewable diesel alternative with a longer commercial history, is produced through the transesterification of vegetable oils, animal fats, or waste cooking oils, resulting in fatty acid methyl esters (FAMEs) [5]. Unlike BHD, biodiesel contains polar molecules with oxygen-containing functional groups that enhance boundary lubrication properties through stronger adhesion to metal surfaces [6]. The unique molecular structure of biodiesel, featuring both polar (oxygen-containing) and non-polar (hydrocarbon chain) regions, enables excellent miscibility and compatibility with various fuel types, making it an ideal blending component for improving fuel properties across different petroleum and renewable fuel systems [2]. This polarity creates a protective film that reduces friction and wear between metal components in fuel systems [6]. Additionally, biodiesel typically exhibits a higher specific gravity compared to BHD, which contributes to improved fuel density characteristics. When strategically blended with BHD, biodiesel serves dual purposes: its polar nature enhances the fuel–metal adhesion at the molecular level while simultaneously improving the overall specific gravity of the blended fuel to within the acceptable range specified for conventional diesel engines (0.81–0.87 according to ASTM D975) [7]. These complementary properties make biodiesel an ideal blending component to mitigate the lubrication deficiencies of BHD while maintaining most of the advantageous properties of both fuels, such as high energy content and favorable cold flow behavior.

High-frequency reciprocating rig (HFRR) testing provides valuable insights into the immediate lubricity characteristics of fuels. However, it represents only a simplified, short-duration simulation of actual engine conditions [8]. Advanced tribological testing frameworks have demonstrated that friction force, wear rate, and lubrication performance are interdependent parameters that must be evaluated simultaneously under realistic operating conditions [9]. Long-term testing is essential to comprehensively evaluate the wear behavior of BHD–biodiesel blends under realistic operating environments for several critical reasons. First, actual engine operation involves dynamic temperature variations, pressure fluctuations, and mechanical stresses that cannot be adequately replicated in standard laboratory tests. Second, the stability of biodiesel's lubricity-enhancing properties may deteriorate over time due to oxidation and polymerization processes [10], potentially compromising its long-term wear protection capabilities when blended with BHD. Third, the interactions between fuel components and engine materials evolve gradually, with surface chemistry changes and deposit formation that may only become apparent after extended periods of operation. Fourth, the performance of fuel injector systems, particularly those with high-precision components operating under extreme pressures in modern common rail systems, requires prolonged evaluation to accurately assess component durability and maintenance intervals [4]. Therefore, conducting extended duration tests using actual engine hardware or specialized long-term wear rigs represents a crucial next step in validating the viability of BHD–biodiesel blends for commercial applications.

Previous studies investigating the tribological characteristics of BHD–biodiesel blends have demonstrated promising results regarding the potential of biodiesel as an effective lubricity enhancer for BHD, with several researchers exploring various blending ratios

and their effects on wear mechanisms under controlled laboratory conditions. A previous study [2] evaluated the influence of hydrotreated vegetable oil, also known as BHD fuel, and its palm oil biodiesel blends using HFRR testing, demonstrating that fuel lubricity improved with increasing biodiesel content, as evidenced by reduced wear scar diameter and enhanced film formation percentage. The authors attributed these improvements to the polar nature of biodiesel, which facilitates fuel adsorption on metal surfaces, and its higher viscosity, which promotes the formation of thicker boundary films between HFRR specimens. Similar trends were reported by Sriprathum et al. [11], who investigated various ratios of BHD and palm oil-derived biodiesel using HFRR methodology in accordance with ISO 12156-1 (2018) standards [12], indicating that the polar chemical composition of biodiesel significantly enhanced fuel lubricity when blended with the non-polar paraffinic hydrocarbons characteristic of BHD. Notably, the addition of 5% biodiesel reduced the wear scar diameter from 609 μm to 249 μm, demonstrating the substantial lubricity benefits achievable even with minimal biodiesel content. However, both studies relied exclusively on HFRR testing; therefore, long-term operational studies are necessary to fully understand the performance implications under real-world conditions and validate these laboratory findings in practical applications.

Despite growing research on BHD–biodiesel blends, critical knowledge gaps exist in their long-term tribological behavior under real operating conditions. Current literature primarily features short-duration laboratory tests that inadequately represent the complex wear processes occurring in diesel engines over extended periods. The molecular interactions between BHD and biodiesel at metal interfaces during prolonged exposure remain poorly understood, creating uncertainty about the stability of lubricity enhancements. While the immediate benefits of biodiesel addition to BHD have been documented, limited research addresses optimal blending ratios that balance improved lubricity with oxidation stability, cold flow performance, and energy content during extended operation.

This study aims to address these gaps through comprehensive long-term wear testing of various BHD–biodiesel blends. An experimental investigation was conducted by preparing proportionally blended fuels between BHD and biodiesel (specifically detailed in Section 2) and neat diesel. Chemical composition, fuel properties, engine torque variations, and wear were analyzed. In addition, the visual appearance of engine parts under lubricant contamination (100 and 200 h tests) was also examined and discussed. Specifically, engine part clearance and weight loss were used to measure the engine wear. Furthermore, Fourier-transform infrared spectroscopy analysis was conducted on the carbon deposits accumulated on the piston surfaces to evaluate the chemical characteristics of the combustion residues. This study proposes a performance–wear correlation that provides practical guidelines for long-term operation.

2. Experimental Methodology

2.1. Fuel Preparation

For this study, diesel fuel containing 7% FAMEs was obtained from a standard commercial gas station operating under the Petroleum Authority of Thailand network and was used as the baseline fuel. Commercial-grade palm-based bio-hydrogenated diesel fuel was supplied by Veerasuwan Company Limited, Samutsakorn, Thailand. The commercial-grade biodiesel used in this study was provided by BBGI Public Company Limited, Phra Nakhon Si Ayutthaya, Thailand, a specialized manufacturer that produces biodiesel for government blending programs. Blend fuels were obtained by mixing 90% BHD with 10% biodiesel and 70% BHD with 30% biodiesel by volume, designated as BHD90 and BHD70, respectively. The mixtures were stirred using a magnetic stirrer at 450 rpm to ensure thorough mixing. Appearances of the test fuels are shown in Figure 1.

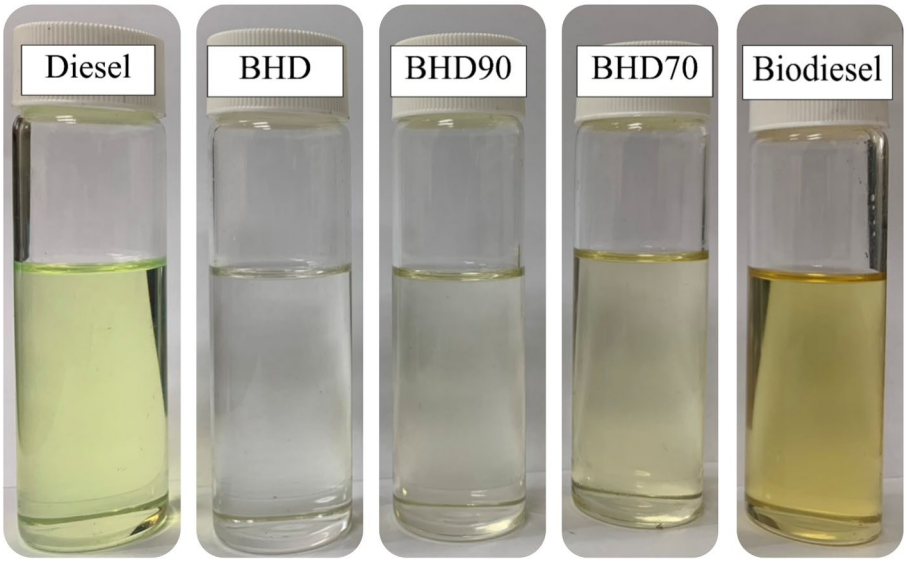


Figure 1. Appearance of the test fuels.

2.2. Fuel Chemical Composition

2.2.1. Gas Chromatography and Mass Spectrometer

A BRUKER GC-MS/Series 3XO gas chromatography–mass spectrometer (Bruker Corporation, Goes, The Netherlands) equipped with a DB-wax capillary column (0.25 mm inner diameter, 60 m length, 0.25 μm film thickness) was used to identify the chemical composition of diesel fuel and BHD. Helium was used as the carrier gas with a steady flow rate of 1.0 mL/min in the test method details. The oven temperature was initially held at 70 °C for 3 min, then ramped at 3 °C/min to 180 °C, followed by a 10 °C/min ramp to 250 °C, which was maintained for 25 min. The split ratio was 20:1, and the inlet was maintained at 250 °C. Each sample received a 1 μL injection volume. The mass spectrometer source was set at 250 °C, and scanning was performed over a mass-to-charge ratio (m/z) range of 35 to 550.

For the chemical composition analysis of biodiesel, an Agilent 7890A gas chromatography (GC) (Agilent Technologies, Wilmington, DE, USA) with a CP-Sil 88 column (100 m length × 0.25 mm inner diameter, 0.20 μm film thickness) was used. Helium was used as the carrier gas at a constant flow rate of 0.38 mL/min. The oven temperature program started at 70 °C for 4 min, ramped at 13 °C/min to 175 °C (held for 27 min), then at 4 °C/min to 215 °C (held for 15 min), and finally at 4 °C/min to 240 °C (held for 12 min). The injection volume was set at 1 μL for each sample, and the inlet temperature was kept at 250 °C with a 50:1 split ratio. The chromatograms of diesel, BHD, and biodiesel are provided in Figures S1–S3 in the Supplementary Material; their detailed chemical compositions were reported in our previous work [13,14].

2.2.2. Fourier-Transform Infrared Spectrometer

To analyze the complicated functional groups of diesel, BHD, and biodiesel fuels, an attenuated total reflectance Fourier-transform infrared (ATR-FTIR) spectrometer (Bruker Corporation, Ettlingen, Germany), model TENSOR 27-Hyperion-2000 was employed. The analysis covered a spectral range between 450 and 4000 cm^{-1}.

For carbon deposit analysis, samples were collected from accumulated deposits on piston tops after the 200 h engine durability test. Sample analysis was performed using an FTIR spectrometer (Tensor 27, Bruker Optics, Ettlingen, Germany) equipped with a deuterated triglycine sulfate detector system. Measurements were conducted using a diamond ATR crystal accessory capable of measuring infrared absorption in the spectral

range of 4000–400 cm^{-1} (Bruker Optics, Ettlingen, Germany). The instrument operation was controlled using OPUS 7.5 software, with parameters set at a resolution of 4 cm^{-1} and 64 scans per measurement. Each sample was measured in triplicate, with 3 spectra collected per replicate, yielding a total of 9 spectra per sample. The integrated peak areas of various functional groups were analyzed to enable quantitative comparison of compositional differences among samples.

2.3. Fuel Properties Test

The chemical and physical properties of all test fuels, including commercial diesel, were evaluated using standardized ASTM test methods. Each property was measured in triplicate, and only average values are reported. Kinematic viscosity at 40 °C was measured using a Cannon-Fenske viscometer (CANNON Instrument Company, Pennsylvania, PA, USA) in accordance with ASTM D445 by recording the time required for a fixed volume of fuel to flow through a calibrated glass capillary under gravity [15]. Density and specific gravity at 15.6 °C were determined using a hydrometer following ASTM D1298 [16]. The instrument was immersed in the fuel sample, and readings were taken after reaching thermal equilibration. The higher heating value was measured using a LECO AC600 bomb calorimeter (LECO Corporation, St. Joseph, MI, USA) as specified by ASTM D240 by combusting a known mass of fuel under pure oxygen in a sealed vessel and recording the released heat [17]. Distillation characteristics, specifically the 50% recovery temperature, were assessed using automated distillation equipment following ASTM D86 [18]. The fuel was heated at a controlled rate, and the temperature at which 50% of the sample volume evaporated and condensed was recorded. The cetane index was subsequently calculated from the measured density and 50% recovery temperature data according to ASTM D976 [19]. The flash point was determined using a closed cup tester as prescribed by ASTM D93 [20]. The fuel sample was heated at a controlled rate, and the lowest temperature causing vapor ignition upon exposure to a small flame was recorded. Fuel lubricity was evaluated using a high-frequency reciprocating rig in accordance with ISO 12156-1. A steel ball was oscillated against a steel disc submerged in the fuel sample under defined conditions (load, frequency, and temperature) for 75 min. The resulting wear scar diameter on the ball was then measured as an indicator of lubricity. The analyzed fuel properties are summarized in Table 1.

Table 1. Physiochemistry of the test fuels.

Fuel Properties	Test Method	Limit [21]	Diesel	BHD	BHD90	BHD70	FAME
Kinemetric Viscosity at 40 °C (cSt)	ASTM D445	1.8–4.1	3.12	2.58	2.65	2.8	5.16
Specific Gravity at 15.6 °C	ASTM D1298	0.81–0.87	0.83	0.77	0.788	0.815	0.875
API Gravity at 15.6 °C	ASTM D1298	-	39	52	48	42	30
Density at 15.6 °C (kg/m^3)	ASTM D1298	-	829	769	787	814	874
Cetane Index	ASTM D976	>50	56	78	70	60	48
Gross Calorific Value (MJ/kg)	ASTM D240	-	43.48	47.02	46.26	44.54	39.62
Flash Point (°C)	ASTM D93	>52	78	87	86	90	169
Wear Scar Diameter (µm)	ISO 12156-1	<460	220	570	180	180	180
Distillation Temperature	ASTM D86						
Initial Boiling Point (°C)			182	158	162	174	302
10% Recovered (°C)			222	220	226	232	336
50% Recovered (°C)			280	258	262	270	356
90% Recovered (°C)		<357	334	274	288	314	374
Final Boiling Point (°C)			336	282	300	318	376

2.4. Test Engine Setup

Long-term engine wear assessment was conducted using a 200 h protocol under constant load conditions in accordance with Thai Industrial Standard (TIS 2618-2557) [22], as illustrated in Figure 2. Initially, the engine underwent disassembly, with critical components including pistons, rings, valves, crankshaft, and wrist pins being weighed and photographically documented. Following reassembly, baseline performance measurements (torque and power at designated speeds) were recorded. The engine was then operated until reaching normal operating temperature (approximately 80 °C lubricant temperature). Following the TIS 2618-2557 standard, the engine was run at 3000 rpm with a 10 m head load and a 557 L/min water flow rate for 3 h intervals. Daily operation consisted of four 3 h cycles (12 h total) with mandatory 1 h rest periods between cycles, continuing until the full 200 h test duration was completed. Lubricating oil samples were collected at 100 and 200 operating hours for analysis. Upon test completion, performance parameters were reassessed before disassembly and comparative weighing of the previously documented components. The testing protocol adhered to the manufacturer's service specifications for a stock engine configuration. Lubricating oil was initially replaced after the 20 h run-in period, after which the engine continued to operate until it reached the 200 h mark.

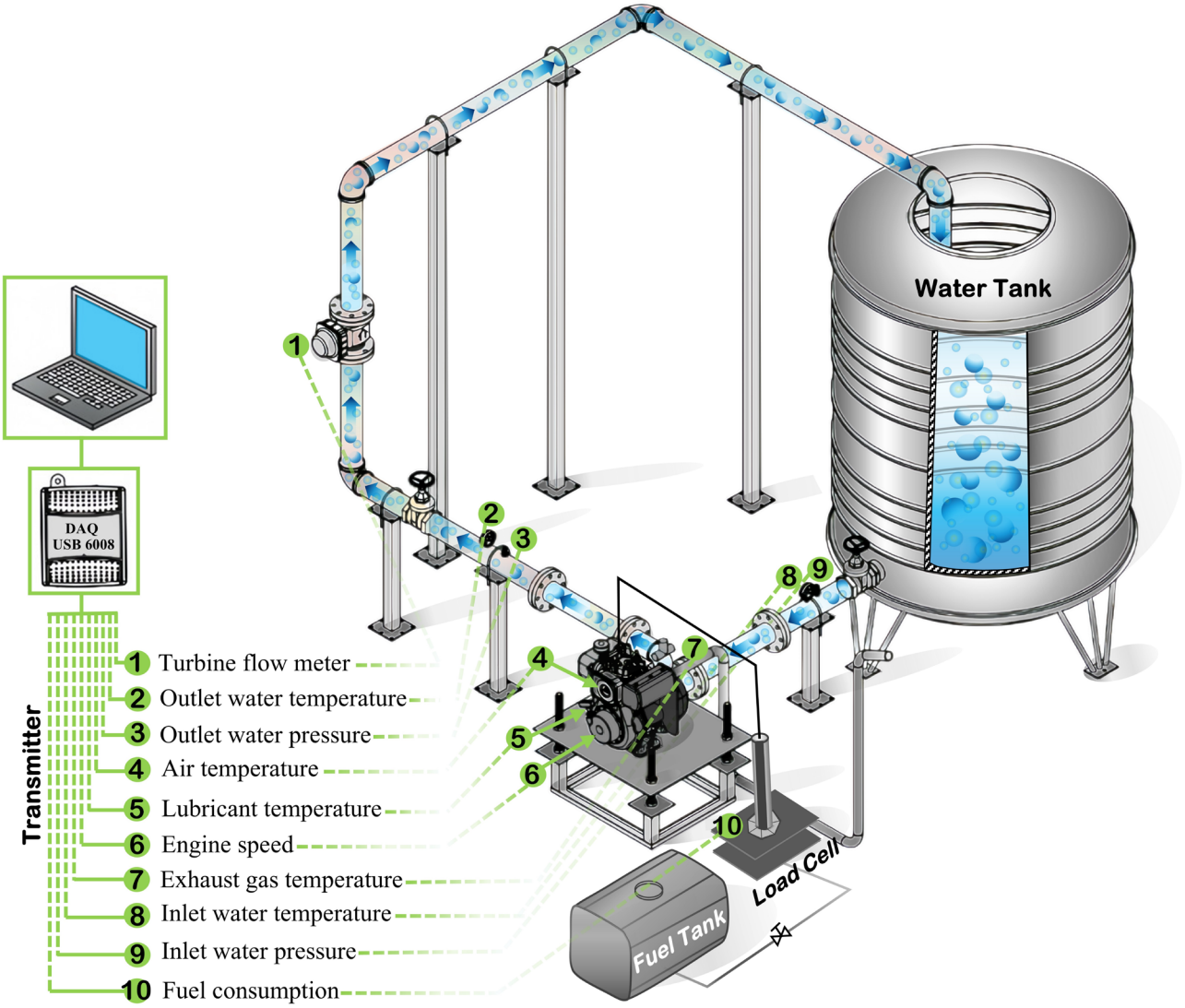


Figure 2. Schematic diagram of the engine setup used for the long-term test.

Oil samples underwent comprehensive analysis for wear particles, physical properties, and contamination through an independent third-party laboratory using established analytical techniques. All measurements were conducted in triplicate, with mean values reported in this study. Fine metallic particles (less than 3 μm) were quantified using inductively coupled plasma–atomic emission spectrometry (ICP-AES). In this technique, the oil sample was nebulized and introduced into a high-temperature argon plasma, causing the metallic elements to emit characteristic wavelengths of light that were detected and quantified by an emission spectrometer (Avio 200, PerkinElmer Inc., Waltham, MA, USA). Coarse metallic debris (5–100 μm) was analyzed via rotrode filter spectroscopy–atomic emission spectrometry (RFS-AES). The oil sample was passed through a rotating filter electrode, where large metallic particles were captured, then vaporized, and analyzed by atomic emission spectrometry to determine elemental concentrations. The metallic elements examined included iron, chromium, lead, copper, tin, aluminum, nickel, silver, molybdenum, and titanium. To encompass larger particle sizes, ferrous particle quantification utilized the PQ Index methodology, which measures ferrous metallic particles ranging from 3 to 1000 μm in oil samples. This dimensionless index represents the ratio of ferrous particle mass to oil mass. Physical oil characteristics, including kinematic viscosity at 100 °C, total base number (TBN), oxidation levels, and nitration, were assessed according to ASTM standards D445, D4739, D7414, and D7624 [23–25], respectively. Contamination analysis encompassed water content (ASTM D95) and carbon deposit levels (ASTM D7844) [26], while fuel dilution in the lubricant was measured through surface acoustic wave (SAW) methodology. Engine components were evaluated using digital instrumentation capable of microgram resolution for mass and micrometer resolution for dimensions.

3. Results and Discussion

3.1. Chemical Composition

The detected chemical compositions and their carbon ranges are presented in Tables 2 and 3, respectively. Diesel fuel contains hydrocarbons distributed across three carbon ranges: C_6–C_{12} (12.09%), C_{13}–C_{18} (61.73%), and >C_{18} (26.18%). The identified compounds within these ranges include alkanes, alkenes, and fatty acid methyl esters (FAMEs). The presence of FAMEs in commercial diesel is not inherent to petroleum refining. Rather, it results from the mandatory blending of palm oil-derived biodiesel into commercial diesel fuel, as required by the fuel quality standards announced by the Department of Energy Business, Ministry of Energy, Thailand [21]. Diesel fuel generally contains longer-chain hydrocarbons (C_{13}–C_{18} and >C_{18}), dominated by saturated hydrocarbons and a small proportion of unsaturated hydrocarbons and oxygenated compounds. While longer hydrocarbon chains can slightly enhance viscosity and film strength, the overall lubricity of diesel mainly benefits from trace polar or oxygenated components rather than chain length alone [3,27].

In contrast, BHD is dominated by C_{13}–C_{18} hydrocarbons (85.29%) with minor C_6–C_{12} fractions (13.73%) and trace aromatics (0.98%). This fuel is almost entirely composed of alkanes with non-polar structures. The absence of polar oxygenated species removed during the hydrotreatment process was reported to reduce lubricity due to weaker surface adsorption on metallic surfaces [3,27]. This confirms that fatty acids from the palm oil feedstock were successfully converted into saturated hydrocarbons during the hydrogenation process.

Biodiesel, by contrast, exhibits a highly concentrated composition of C_{13}–C_{18} FAME (98.99%) alongside minimal shorter (C_6–C_{12}: 0.42%) and longer-chain (>C_{18}: 0.59%) fractions. The consistent ester functional groups in FAME molecules contribute to their polar nature and strong adsorption on metallic surfaces, improving boundary lubrication and reducing friction. Therefore, the high C_{13}–C_{18} FAME content in biodiesel is expected to

provide superior lubricity compared with diesel and BHD, potentially mitigating engine wear under suitable operating conditions [2,28].

Table 2. Detected compositions from base fuels sorted by carbon number.

Carbon Number	Weight Percentage (%)		
	Diesel	BHD	Biodiesel
C6:0			
C7:0		0.03	
C8:0		0.50	0.03
C9:0		0.07	
C10:0	2.67	1.13	0.03
C11:0	4.19	4.27	
C12:0	5.23	7.73	0.35
C13:0	6.50	5.22	
C14:0	5.58	12.02	1.00
C14:1	1.85		
C15:0	5.45	25.21	0.05
C16:0	18.94	42.65	37.92
C16:1			0.19
C17:0	5.78	0.17	0.09
C18:0	5.66	0.02	4.13
C18:1	9.90		43.94
C18:2	2.08		11.48
C18:3			0.19
C19:0	7.27		
C20:0	4.30		0.33
C20:1			0.13
C21:0	3.51		
C22:0	2.76		0.06
C23:0	2.54		
C24:0	1.90		0.07
C25:0	1.54		
C26:0	1.20		
C27:0	0.80		
C28:0	0.36		
Aromatic		0.98	

Table 3. Carbon range distribution of base fuels.

Carbon Range	Area Percentage (%)		
	Diesel	BHD	Biodiesel
C_6–C_{12}	12.09	14.56	0.42
C_{13}–C_{18}	48.65	85.44	98.99
>C_{18}	39.26	0.00	0.59

The FTIR spectra of diesel, BHD, and biodiesel are shown in Figure 3, and the identified functional groups are summarized in Table 4. Diesel, which contains a 7% FAME blend, predominantly exhibits characteristic C–H stretching vibrations at 2955, 2922, and 2854 cm^{-1}, and C–H bending modes at 1460 and 1377 cm^{-1}. The absorption at 722 cm^{-1} corresponds to C–H rocking, confirming the presence of long-chain hydrocarbons typical of petroleum-based fuels. A small carbonyl (C=O) stretching peak at 1745 cm^{-1} indicates ester functionality from the blended FAME component, confirming that this fuel is a biodiesel blend rather than pure petroleum diesel.

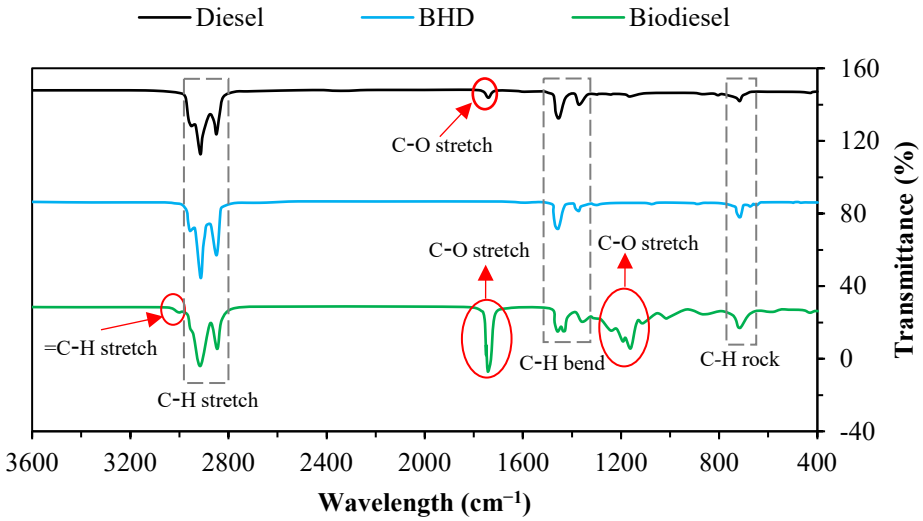


Figure 3. Functional group characterization of oil samples by FTIR analysis.

Table 4. Summary of the functional group analysis of pure base fuels.

Wavelength (cm^{-1})			Frequency of Wavelength (cm^{-1})	Vibration Type	Functional Group
Diesel	BHD	Biodiesel			
-	-	3005	3100–3000	=C–H stretch	alkenes
2955	2957	-	3000–2850	C–H stretch	alkane
2922, 2854	2921, 2853	2923, 2853	3000–2850	C–H stretch	alkane
1745	-	1742	1760–1740	C=O stretch	carbonyl
1460	1463	1462, 1437	1470–1450	C–H bend	alkanes
1377	1377	1360	1590–1360	C–H bend	alkanes
-	-	1196, 1169	1250–1150	C–O stretches	carbonyl
-	-	1016	1100–1000	C–O stretches	carbonyl
722	721	722	730–675	C–H rock band	alkenes
-	-	849	1000–650	=C-H bend	alkenes
-	678	-	900–675	=C-H bend	aromatic

BHD presents a similar alkane profile with C–H stretching at 2957, 2921, and 2853 cm^{-1} and C–H bending at 1463 and 1377 cm^{-1}. The band at 721 cm^{-1} also signifies long hydrocarbon chains. In addition, a weak peak at 678 cm^{-1}, assigned to aromatic =C–H bending, suggests the presence of aromatic hydrocarbons. This observation aligns with GC-MS analysis studies [29], which reported aromatic compounds in hydrotreated vegetable oil. The absence of a carbonyl peak confirms that BHD consists purely of hydrocarbons without ester content, distinguishing it from the FAME-blended diesel.

Biodiesel shows characteristic ester absorption bands consistent with its fatty acid methyl ester composition. A strong carbonyl (C=O) stretching vibration appears at 1742 cm^{-1}, accompanied by multiple C–O stretching bands at 1196, 1169, and 1016 cm^{-1}. Similar to other fuels, biodiesel exhibits C–H stretching at 2923 and 2853 cm^{-1} and bending at 1462, 1437, and 1360 cm^{-1}. However, biodiesel uniquely presents unsaturation bands, with =C–H stretching at 3005 cm^{-1} and =C–H bending at 849 cm^{-1}. The pronounced intensity of the carbonyl peak in pure biodiesel compared with the minor peak in the 7% FAME-blended diesel clearly indicates its higher ester content. Overall, the IR spectra clearly differentiate the hydrocarbon-dominant BHD from the ester-containing biodiesel and FAME-blended diesel, consistent with their chemical structures and compositional analyses.

3.2. Fuel Properties

The kinematic viscosity measurements at 40 °C revealed significant variations among test fuels that could directly influence lubrication performance and fuel atomization during extended engine operation. BHD exhibited the lowest viscosity at 2.58 cSt, followed by the blends BHD90 (2.65 cSt) and BHD70 (2.80 cSt), compared to diesel's 3.12 cSt and biodiesel's 5.16 cSt. All test fuels remained within the ASTM D975 specification range of 1.8–4.1 cSt, though BHD's reduced viscosity may introduce inadequate fuel system lubrication during long-term operation [30]. The progressive viscosity increases from BHD to BHD90 to BHD70 demonstrated biodiesel's effectiveness in improving fuel film thickness, with BHD70 approaching diesel's viscosity characteristics, while BHD90 provided intermediate lubrication enhancement. This viscosity progression directly correlated with the measured wear scar diameter results, where both BHD90 and BHD70 achieved superior lubricity performance at 180 μm compared to BHD's poor 570 μm and diesel's moderate 220 μm, confirming that even a 10% biodiesel addition significantly improved boundary lubrication properties [31].

Specific gravity measurements revealed a systematic fuel density progression that influences fuel injection characteristics and engine compatibility. BHD showed the lowest specific gravity at 0.770, with blends BHD90 (0.788) and BHD70 (0.815) progressively approaching diesel's value of 0.830, while biodiesel exhibited the highest density at 0.875. All test fuels fell within the ASTM D975 specification range of 0.81–0.87, except for pure BHD, which slightly undershot the minimum requirement. The corresponding density values (BHD: 769 kg/m^3, BHD90: 787 kg/m^3, BHD70: 814 kg/m^3, diesel: 829 kg/m^3, biodiesel: 874 kg/m^3) demonstrated how biodiesel blending effectively adjusted BHD's density characteristics toward conventional diesel specifications. This density improvement with increasing biodiesel content enhances fuel injection spray characteristics and combustion efficiency, as reflected in the API gravity progression from BHD's high 52° to diesel's moderate 39° and biodiesel's low 30°.

The higher heating value analysis revealed energy density differences that directly influenced engine performance throughout long-term testing. BHD demonstrated the highest energy content at 47.02 MJ/kg, with blends showing progressive reduction: BHD90 (46.26 MJ/kg) and BHD70 (44.54 MJ/kg), approaching diesel's 43.48 MJ/kg and exceeding biodiesel's lowest value of 39.62 MJ/kg. This energy hierarchy suggested that BHD blends could maintain superior power output potential while benefiting from biodiesel's lubrication enhancements, with BHD90 providing an optimal balance between energy density and enhanced component protection during extended engine operation [32].

Cetane index measurements revealed exceptional combustion quality differences that could influence engine wear patterns and deposit formation during extended operation. BHD exhibited the highest cetane index of 78, with blends BHD90 (70) and BHD70 (60) maintaining excellent ignition characteristics, compared to diesel's 56 and biodiesel's 48. All fuels, except pure biodiesel, remained well above the minimum specification of 50. BHD and its blends, primarily composed of paraffinic hydrocarbons, exhibited high cetane numbers that resulted in shorter ignition delay periods and more controlled combustion through improved fuel–air mixing [33], potentially reducing engine stress and deposit formation during extended operation. This superior combustion quality suggested cleaner burning characteristics that could lead to reduced carbon deposit formation and lower combustion-related contamination in engine oil during extended testing.

Distillation temperature analysis revealed distinct volatility patterns affecting fuel atomization and combustion behavior during long-term engine operation. BHD exhibited the most favorable distillation curve with an initial boiling point at 158 °C, 50% recovery at 258 °C, and a final boiling point at 282 °C, indicating excellent volatility characteris-

tics. The blends showed progressive temperature increases: BHD90 (initial: 162 °C, 50%: 262 °C, final: 300 °C) and BHD70 (initial: 174 °C, 50%: 270 °C, final: 318 °C), approaching diesel's profile (initial: 182 °C, 50%: 280 °C, final: 336 °C) while remaining well below biodiesel's high temperatures (initial: 302 °C, 50%: 356 °C, final: 376 °C). All 90% recovery temperatures remained below the ASTM specification limit of 357 °C, with BHD blends showing intermediate characteristics that balanced improved volatility from BHD with enhanced lubricity from biodiesel addition, directly influencing fuel atomization quality and combustion completeness during the extended engine testing [30].

3.3. Analysis of Engine Torque Variations and Their Implications

Prior to the commencement of the 200 h durability test, all engines demonstrated comparable torque output characteristics across the tested fuel types, as shown in Figure 4. The initial torque values ranged from 25.13 N·m (biodiesel) to 26.57 N·m (BHD90). Despite BHD having the highest gross calorific value among the test fuels (47.02 MJ/kg), its baseline torque of 25.84 N·m was slightly lower than that of diesel (26.30 N·m), which can be attributed to BHD's lower density (769 kg/m^3 vs. 829 kg/m^3 for diesel), resulting in a reduced mass of fuel delivered per injection cycle. BHD90 produced the highest baseline torque at 26.57 N·m, as the addition of 10% biodiesel improved fuel density toward the conventional diesel range while retaining a high energy content. BHD70 and biodiesel yielded baseline torques of 25.49 N·m and 25.13 N·m, respectively, with biodiesel producing the lowest value due to biodiesel's lower calorific value of 39.62 MJ/kg [34]. These pre-test measurements confirmed that all engines were operating within normal performance parameters and provided a consistent foundation for evaluating the long-term effects of fuel lubricity properties on engine durability and performance retention.

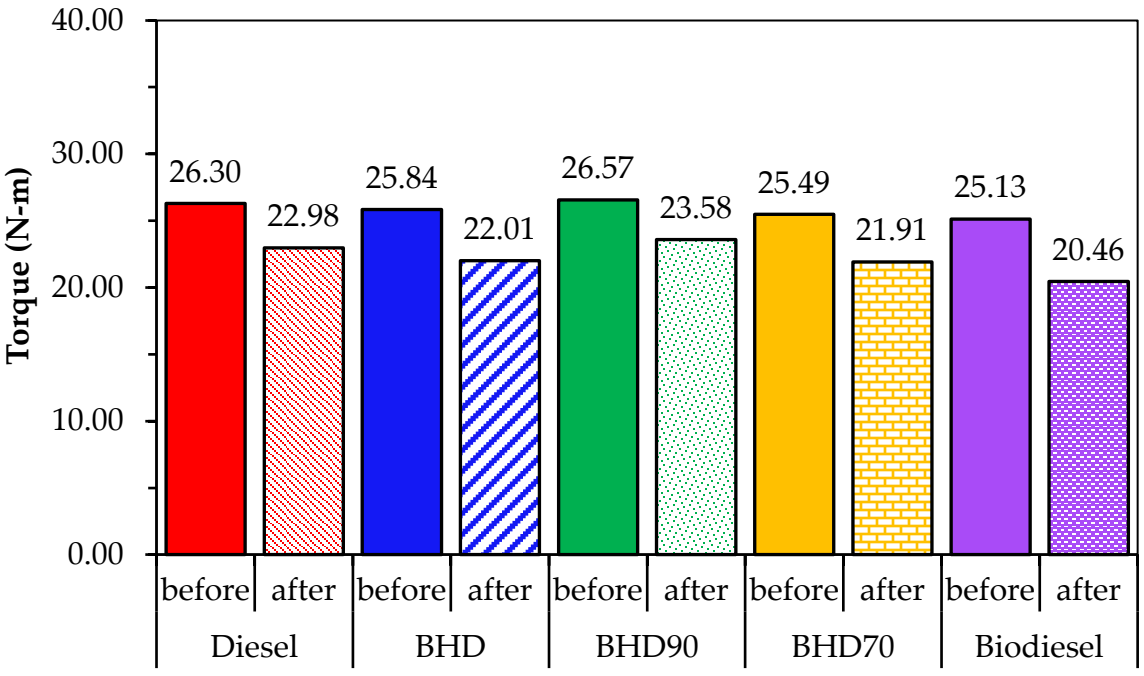


Figure 4. Engine torque before the 200 h test and the corresponding torque reductions after the test.

Following the completion of the 200 h durability test, torque reductions were observed across all fuel types, with the magnitude of performance loss reflecting the differences in fuel lubricity properties and lubrication system condition among the test fuels. BHD90 engines achieved the best performance retention, declining from 26.57 to 23.58 N·m (2.98 N·m reduction, 11.2%), demonstrating the protective effect of 10% biodiesel blending in mitigating wear-related performance losses through improved boundary lubrication. Diesel-fueled

engines experienced a reduction from 26.30 to 22.98 N·m (3.32 N·m reduction, 12.6%), representing moderate performance degradation consistent with normal long-term engine wear expectations. BHD70 engines showed a reduction from 25.49 to 21.91 N·m (3.58 N·m reduction, 14.0%), while BHD engines demonstrated a notable performance decline, dropping from 25.84 to 22.01 N·m (3.83 N·m reduction, 14.8%), directly reflecting the inadequate lubricity properties that resulted in excessive component wear, increased clearances, and reduced compression efficiency. Biodiesel demonstrated the most severe decline from 25.13 to 20.46 N·m (4.68 N·m reduction, 18.6%), attributed to accelerated lubricant oxidation caused by biodiesel's hygroscopic properties, which promoted water accumulation through blow-by gases and subsequent oxidative degradation of the lubricant system [35].

3.4. Engine Wear

3.4.1. Engine Part Clearance and Weight Loss

The 200 h engine component analysis revealed significant weight loss patterns that directly correlated with fuel lubricity properties and engine wear severity. Engine part weight loss and clearance are shown in Tables 5 and 6, respectively. BHD-operated engines demonstrated severe component degradation across all measured parts, while higher biodiesel blends showed even more concerning material loss patterns. The first compression ring weight loss varied among the test fuels as follows: diesel (0.0290 g), BHD (0.0347 g), BHD90 (0.0246 g), BHD70 (0.0463 g), and biodiesel (0.0602 g). Compared to diesel, BHD showed a 19.7% increase, and BHD90 demonstrated a 15.2% reduction, while BHD70 and biodiesel exhibited significant increases of 59.7% and 107.6%, respectively. The second compression rings followed similar degradation patterns, with BHD showing 0.0326 g of weight loss, BHD70 experiencing 0.0473 g (72.0% greater than diesel), and biodiesel demonstrating the most severe loss at 0.0611 g (122.2% greater than diesel), while BHD90 maintained exceptional retention at 0.0148 g (46.2% better protection than diesel). The oil control rings showed progressive wear escalation, with BHD at 0.0261 g, BHD70 at 0.0281 g, and biodiesel at 0.0285 g, all exceeding diesel's 0.0246 g and BHD90's superior 0.0211 g performance. Most critically, the fuel pump tappet components demonstrated extreme lubricity-related wear progression, with BHD engines experiencing 0.0181 g of weight loss, BHD70 showing 0.0239 g (97.5% greater than diesel), and biodiesel reaching 0.0260 g (114.9% greater than diesel), compared to diesel's 0.0121 g and BHD90's minimal 0.0074 g, confirming the direct relationship between fuel composition and component protection. Piston weight measurements revealed the most dramatic material loss escalation, with BHD engines losing 0.95 g, BHD70 experiencing 1.19 g (35.2% greater than diesel), and biodiesel showing a catastrophic loss of 1.62 g (84.1% greater than diesel), versus diesel's 0.88 g and BHD90's exceptional 0.76 g performance.

Engine clearance measurements after 200 h of operation revealed critical dimensional changes that directly impacted engine performance and compression characteristics, with higher than 10% biodiesel blends showing the most severe degradation patterns, which correlated with previous work HFRR results [11]. The cylinder liner dimensional analysis revealed a clear progression of wear severity: BHD causing 0.0085 mm wear depth (22.4% greater than diesel), BHD70 showing 0.0098 mm depth (41.2% greater than diesel), and biodiesel demonstrating the most severe wear at 0.0112 mm (61.4% greater than diesel), compared to diesel's 0.00694 mm and BHD90's superior 0.00328 mm performance (52.7% better protection than diesel). A similar trend was reported by Gupta and Agarwal (2021) [36]. Piston clearance measurements confirmed this degradation pattern, with BHD and BHD70 both showing −0.076 mm changes and biodiesel reaching −0.083 mm, compared to diesel's −0.038 mm and BHD90's optimal −0.026 mm performance. These dimensional changes directly supported the metal particle analysis findings and explained

the observed engine performance degradation, as increased clearances led to reduced compression efficiency and accelerated lubricant contamination that perpetuated the wear cycle throughout the extended operational period. The detailed metal particle contamination analysis and lubricant degradation patterns that corroborate these physical measurements will be comprehensively discussed in the following section.

Table 5. Differences in the weight of engine parts before and after the 200 h test.

Component	Differences in Engine Parts Weight Before and After Test (g)				
	Diesel	**BHD**	**BHD90**	**BHD70**	**Biodiesel**
First compression ring	0.0290	0.0347	0.0246	0.0463	0.0602
Second compression ring	0.0275	0.0326	0.0148	0.0473	0.0611
Oil control ring	0.0246	0.0261	0.0211	0.0281	0.0285
Fuel pump tappet	0.0121	0.0181	0.0074	0.0239	0.0260
Piston pin	0.0054	0.0059	0.0047	0.0056	0.0059
Piston	0.8800	0.9500	0.7600	1.1900	1.6200

Table 6. Differences in engine parts size before and after the 200 h test.

Component	Differences in Engine Parts Before and After Test (mm)				
	Diesel	**BHD**	**BHD90**	**BHD70**	**Biodiesel**
Liner	−0.00694	−0.0085	−0.00328	−0.0098	−0.0112
Piston pin	0.0065	0.00717	0.00392	0.0103	0.0111
Piston	0.01933	0.02417	0.01417	0.0337	0.0367
Intake valve	0	0	0	0	0
Exhaust valve	0	0	0	0	0
Piston Clearance	−0.038	−0.076	−0.026	−0.076	−0.083

"−" means a decrease in size.

3.4.2. Performance–Wear Correlation and Long-Term Implications

The relationship between measured engine wear and torque performance degradation provided critical insights into the long-term viability of alternative fuel systems in commercial applications. The 14.8% torque reduction in BHD engines directly corresponded with the 36.4% exceedance of iron particle safety limits, 22.4% greater cylinder liner wear, and 100% increased piston clearances compared to diesel operation, demonstrating how lubricity-related component degradation translates to measurable performance losses. BHD90's superior 11.2% torque reduction, despite operating under identical conditions, validated the effectiveness of optimal biodiesel blending as a lubricity enhancement strategy, with the 10% biodiesel component providing sufficient boundary lubrication to maintain acceptable wear rates and preserve engine performance [11]. However, the performance degradation dramatically escalated with higher biodiesel content, as BHD70 and biodiesel engines showed progressively worse performance retention, with the difference between BHD90 and biodiesel reaching 13.4% for torque and 14.4% for power. BHD70 engines demonstrated intermediate performance degradation with moderate torque reduction, while biodiesel engines experienced the most severe performance decline, correlating with their extreme wear patterns, including 114.9% greater fuel pump tappet wear, 84.1% higher piston weight loss, and 61.4% increased cylinder liner wear compared to diesel operation. The catastrophic wear progression from BHD90 through BHD70 to pure biodiesel was attributed to accelerated lubricant oxidation caused by biodiesel's hygroscopic properties, which promoted water accumulation through blow-by gases and subsequent oxidative degradation of the lubricant system [37], ultimately negating the lubricity benefits at higher blending ratios. These findings indicate that while BHD engines would require more

frequent maintenance and component replacements compared to diesel, BHD90 systems demonstrate optimal durability through effective lubricity management, whereas BHD70 and biodiesel blends exceed the threshold where lubricity benefits are overwhelmed by oxidative degradation effects. The strong correlation between fuel composition, component wear, and performance retention highlights the critical importance of optimizing biodiesel blending ratios to balance tribological benefits with oxidation stability in long-term engine reliability and operational costs.

3.5. Visual Appearances of Engine Parts

Tables 7 and 8 show the visual appearance of engine parts after the 200 h long-term durability test. Visual inspection of piston crowns after the 200 h testing revealed distinct carbon deposit formation patterns that correlated with fuel composition and combustion characteristics. BHD demonstrated the cleanest combustion with minimal fine, dry carbon deposits that were easily removable, attributed to its saturated paraffinic structure and absence of aromatic compounds that promote complete combustion [38]. Diesel fuel showed moderate carbon deposit accumulation with dry, fine particles and localized hard carbon deposits on the piston surface. BHD90 exhibited similar clean combustion characteristics to BHD with slightly more carbon deposits, indicating that 10% biodiesel addition maintained combustion efficiency while providing lubricity benefits. However, higher biodiesel blends showed deteriorating combustion quality, with BHD70 displaying increased hard carbon deposits and the appearance of white ash deposits attributed to metallic contaminants (sodium, potassium, calcium, magnesium) from biodiesel impurities. Pure biodiesel demonstrated the most severe deposit formation with substantial hard carbon accumulation and prominent white ash deposits, indicating incomplete combustion despite biodiesel's oxygen content, likely due to poor atomization caused by high viscosity and oxidation-induced polymerization [39]. The carbon deposit formation hierarchy from highest to lowest was biodiesel > BHD70 > diesel > BHD90 > BHD.

Cylinder head examination revealed progressive deposit formation patterns consistent with piston crown observations. BHD showed minimal fine carbon deposits with no hard carbon accumulation, confirming superior combustion quality. BHD90 displayed slight hard carbon deposits around the injector area and intake valve edges but remained predominantly clean with fine, dry carbon deposits. Higher biodiesel blends (BHD70 and biodiesel) showed concerning deposit escalation, with white ash deposits appearing on exhaust valves and throughout the cylinder head area, indicating incomplete combustion and contamination from biodiesel impurities. Fuel injector analysis confirmed these trends, with BHD showing fine, easily removable carbon deposits without hard deposits at the injector tip. BHD90 exhibited minimal hard carbon deposits at the injector tip with fine carbon deposits on the injector body. However, biodiesel demonstrated severe deposit formation with substantial hard carbon accumulation at the injector tip and sheet-like deposits on the injector body, attributed to polymerization reactions caused by heat exposure that increased biodiesel viscosity and promoted incomplete combustion [40].

Intake and exhaust valve inspection provided additional insights into combustion quality differences across the fuel spectrum. BHD maintained the cleanest valve surfaces with minimal wet carbon deposits on intake valves and fine, dry carbon deposits on exhaust valves. BHD90 showed comparable cleanliness with slight hard carbon deposits on exhaust valve stems. Higher biodiesel blends demonstrated progressively worse deposit formation, with BHD70 showing increased dry carbon deposit accumulation on intake valve edges and hard carbon deposits on exhaust valves. Biodiesel exhibited brittle, sheet-like deposits on intake valves and substantial hard carbon deposits on exhaust valves, confirming incomplete combustion patterns. The overall carbon deposit formation confirms that

optimal biodiesel blending (10%) maintained clean combustion, while higher concentrations compromised combustion efficiency despite biodiesel's inherent oxygen content.

Table 7. Visual appearance of pistons and cylinder heads.

Fuel Type	Engine Part		
	Piston (Top)	Piston (Side)	Cylinder Head
Diesel			
BHD			
BHD90			
BHD70			
Biodiesel			

Table 8. Visual appearance of injectors and valves.

Fuel Type	Engine Part		
	Injector	**Intake Valve**	**Exhaust Valve**
Diesel			
BHD			
BHD90			
BHD70			
Biodiesel			

3.6. Lubricant Contamination

3.6.1. The 100 h Test

At the 100 h operational milestone, distinct wear patterns emerged for each fuel type through comprehensive metal particle analysis, revealing a clear progression of wear severity with increasing biodiesel content. The PQ-index, fine metal particle, and coarse metal

particle analyses are shown in Tables 9–11, respectively. The Particle Quantifier Index (PQ Index), a dimensionless parameter that quantifies ferrous metallic particles ranging from 3 to 1000 μm and represents the ratio of ferrous particle mass to oil mass, serves as an early warning indicator for abnormal wear conditions. PQ Index analysis revealed critical early warning signs of abnormal wear, with BHD engines measuring 53 ppm, while BHD70 and biodiesel engines showed dramatically elevated values of 226 ppm and 247 ppm, respectively, far exceeding the 20 ppm standard. Only diesel and BHD90 remained within acceptable limits at 14 ppm each. The severely elevated PQ Index for BHD70 and biodiesel indicated the extensive presence of larger ferrous particles (100–1000 μm), suggesting severe abnormal wear mechanisms, including adhesive wear, abrasive particle generation, and potential micro-seizure events, despite their superior lubricity properties [41]. Fine iron particles (less than 3 μm) showed substantial accumulation with concentrations reaching 72 ppm for diesel, 72 ppm for BHD, and a notably lower 42 ppm for BHD90, but a significantly higher 105 ppm for BHD70 and 150 ppm for biodiesel. While diesel, BHD, and BHD90 remained within the 200 ppm safety threshold, the elevated iron content in BHD70 and biodiesel engines indicated accelerated wear patterns despite biodiesel's inherent lubricity properties. The optimal performance of BHD90 demonstrated the enhanced lubrication properties provided by the 10% biodiesel component, while higher biodiesel concentrations in BHD70 and pure biodiesel showed counterproductive effects. Coarse metal particles (5–100 μm) maintained acceptable concentrations across most fuels: diesel at 22 ppm, BHD at 16 ppm, BHD90 at 16 ppm, BHD70 at 24 ppm, and biodiesel at 20 ppm, all well below the 200 ppm limit, indicating that the primary wear concerns at the 100 h milestone were related to larger particle generation rather than conventional abrasive wear mechanisms.

Table 9. PQ-index and iron particles in engine lubricant oil.

Total Metal Content	Limit (ppm)	Fuel	PTT D3 Plus SAE 40 (Base Oil)	Test Period (h)	
				100	200
PQ-index	<20	Diesel	0	14	50
		BHD	0	53	55
		BHD90	0	14	19
		BHD70	0	226	460
		Biodiesel	0	247	510
Fine iron particles (ICP-AES)	<200	Diesel	0	71.5	159.7
		BHD	0	72	272.8
		BHD90	0	42.4	100.7
		BHD70	0	104.8	150.6
		Biodiesel	0	149.5	229.6
Coarse iron particles (RFS-AES)	<200	Diesel	0	21.5	28.2
		BHD	0	15.9	174.7
		BHD90	0	16.2	26.1
		BHD70	0	22.5	24.2
		Biodiesel	0	20	50.3
ICP + RFS	N/A	Diesel	0	93	187.9
		BHD	0	87.9	447.5
		BHD90	0	58.6	126.8
		BHD70	0	127.3	174.8
		Biodiesel	0	169.5	279.9

Table 10. Contaminated fine metal content in lubricant oil after 100 h and 200 h tests.

Contaminated Metal (PPM)	Limit	PTT D3 Plus SAE 40 (Base Oil)	Diesel		BHD		BHD90		BHD70		Biodiesel	
			100 h	200 h	100 h	200 h	100 h	200 h	100 h	200 h	100 h	200 h
Iron	<200	0	71.5	159.7	72	272.8	42.4	100.7	104.8	150.6	149.5	229.6
Chromium	<15	0	2.9	3.9	2.6	5.2	1.9	3.8	10.1	10.3	4.1	11
Lead	<50	0	0.4	0.8	0.9	0.9	0.2	0.6	0.4	0	0.3	0.5
Copper	<25	0	5.5	7	5	7.1	3.5	6.4	13.1	14.9	13.8	20.7
Tin	<25	0	0	0	0	0	0	0	0.1	0	0	0

Table 11. Contaminated coarse metal content in lubricant oil after 100 h and 200 h tests.

Contaminated Metal (ppm)	Limit	PTT D3 Plus SAE 40 (Base Oil)	Diesel		BHD		BHD90		BHD70		Biodiesel	
			100 h	200 h	100 h	200 h	100 h	200 h	100 h	200 h	100 h	200 h
Iron	<200	0	21.5	28.2	15.9	174.7	16.2	26.1	24.2	22.5	20	50.3
Chromium	<15	0	1.2	0.3	0.2	1.3	0	0.7	4	1.7	0	1.9
Lead	<50	0	0.3	0	0.4	0.2	0	0.8	0	0	0	0
Copper	<25	0	0.9	1	0.6	1	0	0.5	2.7	1.9	1.8	4
Tin	<25	0	0.6	0	1.2	0.7	0	0	0	0.4	0	0

Lubricant analysis at 100 h revealed critical degradation patterns affecting engine protection capabilities, with higher biodiesel blends showing accelerated degradation rates. The comprehensive lubricant property analysis and contamination levels are presented in Tables 12 and 13, respectively. Oxidation levels exceeded acceptable standards for all fuel types, with diesel reaching 11.2, BHD at 9.3, BHD90 at 15.5, BHD70 at 18.6, and biodiesel at 20.8, all surpassing the 8.1 limit and confirming the necessity for scheduled oil changes. The progressive increase in oxidation levels with higher biodiesel content demonstrated the hygroscopic effects and accelerated oxidative degradation associated with increased biodiesel ratios [36]. Kinematic viscosity remained within operational ranges for most fuels but showed concerning increasing trends, with diesel at 13.8 cSt, BHD at 13.8 cSt, and BHD90 at 13.6 cSt, while BHD70 increased to 15.1 cSt and biodiesel reached 17.5 cSt, indicating lubricant thickening from oxidation products. Total base number (TBN) values demonstrated active acid neutralization, with diesel at 9.3 mg KOH/g, BHD at 9.9 mg KOH/g, BHD90 at 9.3 mg KOH/g, BHD70 at 9.66 mg KOH/g, and biodiesel at 7.7 mg KOH/g, with the lower TBN in biodiesel indicating increased acid consumption [42]. Fuel contamination analysis revealed relatively consistent patterns across biodiesel blends, with BHD showing 1.4% fuel dilution, while diesel, BHD90, BHD70, and biodiesel maintained low levels around 0.1%, suggesting that pure BHD's fuel system incompatibilities were mitigated by biodiesel blending. Carbon deposit contamination levels reflected similar combustion efficiency across fuels, with diesel producing 0.52% carbon deposit content, BHD at 0.57%, BHD90 at 0.5%, BHD70 at 0.49%, and biodiesel at 0.57%, indicating relatively clean combustion across all fuel types during this operational period, despite the emerging wear and oxidation challenges.

Table 12. Engine lubricant oil properties after 100 h and 200 h tests.

Properties	Limit	PTT D3 Plus SAE 40 (Base Oil)	Diesel		BHD		BHD90		BHD70		Biodiesel	
			100 h	200 h	100 h	200 h	100 h	200 h	100 h	200 h	100 h	200 h
Viscosity at 100 °C (cSt)	12.5–16.3	14.8	13.8	13.2	13.8	12.3	13.6	11.8	15.1	14.8	17.5	19.7
Oxidation (Abs)	<8.1	4	11.2	17.6	9.3	14	15.5	20	18.6	28	20.8	31.5
Nitration (Abs/cm)	<25	0.4	3.6	5.5	4.4	6.3	3.6	3.5	4.7	5.8	5	7.5
Base Number (mg KOH/g)	>2	7.2	9.3	8.4	9.9	8.2	9.3	6.9	9.66	6.05	7.7	7.54

Table 13. Contamination in engine lubricant oil after 100 h and 200 h tests.

Contamination	Limit	PTT D3 Plus SAE 40 (Base Oil)	Diesel		BHD		BHD90		BHD70		Biodiesel	
			100 h	200 h	100 h	200 h	100 h	200 h	100 h	200 h	100 h	200 h
Water (% wt.)	<0.25	0.08	0.072	0.077	0.062	0.067	0.065	0.069	0.094	0.091	0.1	0.093
Fuel (% wt.)	<5	-	0.1	1.1	1.4	1.4	0.1	1.4	0.1	0.1	0.1	0.1
Carbon Deposit (% wt.)	-	-	0.52	0.86	0.57	0.73	0.5	0.6	0.49	0.59	0.57	0.67
Vanadium (ppm)	<6	0	0	0	0	0	0	0	0	0	0	0
Sodium (ppm)	<30	4	3	4	4	5	1	1	1	3	9	7
Silicon (ppm) *	-	13	19.3	21	15.3	16.7	7.4	8.1	12.5	10.8	22	23.9
Silicon (ppm) **	<50	13	7.7	6.6	5.2	0.4	0	0.4	3.3	0.8	1.9	4.8

* Fine particle, ** coarse particle.

3.6.2. The 200 h Test

The 200 h analysis revealed critical wear acceleration across all fuel types, with a clear progression of severity from optimal to catastrophic performance levels. PQ Index analysis demonstrated the most dramatic changes, with values escalating from the 100 h measurements: BHD90 maintained acceptable levels at 19 ppm (within the 20 ppm standard), diesel increased to 50 ppm (exceeding acceptable limits), BHD reached 55 ppm, while BHD70 and biodiesel showed catastrophic increases to 460 ppm and 510 ppm, respectively, far exceeding safety thresholds and indicating severe abnormal wear mechanisms, including adhesive wear, abrasive particle generation, and potential micro-seizure events. Fine iron particle concentrations increased dramatically, establishing a wear hierarchy: BHD90 maintained superior performance at 101 ppm (within safety limits), diesel showed a manageable increase to 160 ppm, BHD70 escalated to 151 ppm, while BHD engines reached 273 ppm (exceeding the safety threshold by 36.4%), and biodiesel demonstrated the most severe contamination at 230 ppm. The progression from BHD90's slight increase from 100 h levels to biodiesel's 53.6% increase demonstrated how optimal blending (BHD90) provided sustained protection while higher biodiesel content (BHD70, biodiesel) accelerated wear through oxidative degradation mechanisms. Coarse metal particle analysis confirmed the severity hierarchy, with BHD90 (26 ppm) and diesel (28 ppm) remaining well controlled, BHD70 maintaining acceptable levels at 23 ppm, while BHD reached 175 ppm, approaching the danger threshold, and biodiesel escalated to 50 ppm. Chromium contamination patterns reinforced the wear hierarchy, with BHD90 showing 4 ppm, diesel at 4 ppm, BHD70 at 10 ppm, BHD reaching 5 ppm, and biodiesel at 11 ppm, indicating accelerated piston ring wear in higher biodiesel blends and confirming that lubricity benefits were overwhelmed by oxidative degradation effects.

The 200 h lubricant analysis revealed catastrophic degradation of lubrication system integrity across all fuel types, with oxidation levels demonstrating the progressive failure of higher biodiesel blends, with lubricant oil properties and contamination shown in Tables 12 and 13, respectively. Oxidation reached extreme values following the degradation hierarchy: BHD at 14.0, diesel at 17.6, BHD90 at 20.0, BHD70 at 28.0, and biodiesel at the most severe level of 31.5, all drastically exceeding the 8.1 absorption unit standard and indicating complete molecular breakdown proportional to biodiesel content. Kinematic viscosity measurements confirmed severe degradation patterns, with BHD90 experiencing critical viscosity loss to 11.8 cSt below the minimum standard, BHD (12.3 cSt) and diesel (13.2 cSt) maintaining marginally acceptable levels, while BHD70 (14.8 cSt) and biodiesel (19.7 cSt) showed excessive viscosity increases from oxidation polymerization products [43]. Total base number analysis revealed concerning alkaline reserve depletion across the fuel spectrum: diesel at 8.4 mg KOH/g, BHD at 8.2 mg KOH/g, BHD90 at 6.9 mg KOH/g, BHD70 at 6.05 mg KOH/g, and biodiesel at 7.54 mg KOH/g, all approaching the critical 2.0 mg KOH/g minimum threshold, with higher biodiesel blends showing accelerated acid consumption. Fuel contamination patterns revealed system stress indicators, with diesel at 1.1% and BHD and BHD90 both at 1.4%, while BHD70 and biodiesel maintained lower levels at 0.1%, suggesting different degradation mechanisms in extended biodiesel blends. Carbon deposit contamination hierarchy reflected combustion efficiency differences: biodiesel at 0.67%, BHD70 at 0.59%, BHD90 at 0.60%, BHD at 0.73%, and diesel producing the highest levels at 0.86%, though these cleaner combustion characteristics in biodiesel blends were negated by severe oxidative degradation. Nitration levels followed the fuel degradation pattern: BHD90 at 3.5, diesel at 5.5, BHD70 at 5.8, BHD at 6.3, and biodiesel at 7.5, reflecting progressive combustion byproduct contamination that contributed to the overall lubrication system breakdown, enabling the severe wear patterns observed across the fuel spectrum.

The progressive increase in oxidation levels with higher biodiesel content can be mechanistically linked to the water accumulation data presented in Table 13. At 200 h, BHD70 and biodiesel exhibited water content of 0.091% and 0.093% (wt.), respectively, compared to BHD90's lower level of 0.069%, representing increases of 31.9% and 34.8% relative to BHD90. This elevated water accumulation, promoted by biodiesel's hygroscopic nature through blow-by gas absorption, directly corresponded to the substantially higher oxidation levels observed in BHD70 (28.0 Abs) and biodiesel (31.5 Abs) compared to BHD90 (20.0 Abs) at 200 h. The correlation between water content and oxidation rate suggests that each 0.01% increase in water content above BHD90's baseline was associated with approximately a 3.6–4.8 Abs unit increase in oxidation level, which in turn accelerated lubricant degradation and contributed to the elevated iron particle concentrations observed in these blends. This mechanistic linkage confirms that the 10% biodiesel threshold represents the critical point beyond which hygroscopic-induced water accumulation overwhelms the lubricity benefits of biodiesel addition.

Furthermore, the accelerated oxidation in BHD70 and biodiesel blends was reflected in their TBN depletion patterns. At 200 h, BHD70 showed the lowest TBN at 6.05 mg KOH/g, indicating the highest rate of acid-neutralizing capacity consumption. Notably, biodiesel exhibited a relatively high TBN of 7.7 mg KOH/g at 100 h but showed minimal further depletion to 7.54 mg KOH/g at 200 h, despite having the highest oxidation level (31.5 Abs) among all test fuels. This pattern suggests that the lubricant in biodiesel-fueled engines had already undergone severe oxidative degradation by the 100 h mark, consuming a substantial portion of its alkaline reserve in the early stage of operation. Consequently, the reduced rate of TBN consumption between 100 and 200 h does not indicate improved acid neutralization capacity but rather reflects the exhaustion of reactive oxidation substrates as

the lubricant approached complete molecular breakdown. This interpretation is consistent with the catastrophically elevated PQ Index (510 ppm) and fine iron particle concentrations (229.6 ppm) observed in biodiesel-fueled engines at 200 h, confirming that lubricant failure had progressed beyond the point of effective acid management.

3.7. Carbon Deposit Analysis

The FTIR spectra of carbon deposits collected from piston surfaces after the combustion of diesel, BHD, BHD90, BHD70, and biodiesel fuels reveal distinct differences in functional group composition, indicating variations in combustion chemistry and fuel-derived residues. The FTIR spectra of carbon deposits from each fuel type are shown in Figure 5, while their corresponding detected functional groups are presented in Table 14. These spectral signatures provide insights into the chemical nature of deposits formed during the combustion of different fuel blends. Weak absorption peaks at 2918–2845 cm^{-1} were detected in the carbon deposits from diesel and BHD, attributed to aliphatic C–H stretching vibrations, suggesting the presence of long-chain hydrocarbon structures characteristic of unburned or partially oxidized diesel components. These peaks are of relatively low intensity and may not be clearly distinguishable in Figure 5 due to the overlapping of multiple spectra presented in a single plot [44]. Sharp bands around 2361–2363 cm^{-1}, detected in most samples, are assigned to asymmetric stretching of CO_2, likely originating from atmospheric interference or adsorbed combustion gases.

A prominent carbonyl (C=O) stretching vibration appears in all fuel types at approximately 1701–1709 cm^{-1}, indicating the presence of partially oxidized intermediates such as unsaturated aldehydes and ketones. These species are commonly formed through incomplete oxidation of FAMEs in biodiesel and BHD, as well as from fossil diesel components [45]. The spectra also show aromatic C=C stretching bands between 1586 and 1618 cm^{-1}, confirming the formation of polycyclic aromatic hydrocarbons (PAHs), especially in the carbon deposit from BHD and its blends. Weak bending vibrations associated with hydroxyl (O–H) groups were detected around 1378–1440 cm^{-1} in BHD- and biodiesel-derived carbon deposits, reflecting their oxygen-rich molecular structures. These peaks are of relatively low intensity and may not be clearly distinguishable in Figure 5 due to the overlapping of multiple spectra presented in a single plot. Nevertheless, their presence further supports the existence of carboxylic acid derivatives in BHD- and biodiesel-derived carbon deposits.

C–O stretching vibrations detected at 1100–1111 cm^{-1} are notably strong in the carbon deposit from biodiesel and BHD fuels, suggesting retained oxygenated species such as alcohols, esters, or ethers. This finding aligns with the thermal decomposition behavior of biodiesel, which tends to form partially oxidized intermediates under suboptimal combustion conditions. Moreover, the presence of alkenes is indicated by the =C–H bending modes around 959–902 cm^{-1}. Aromatic C–H out-of-plane bending vibrations are also observed at 889–854 cm^{-1}, corresponding to 1,2,4-trisubstituted benzene derivatives, and at 753–758 cm^{-1}, indicative of monosubstituted aromatics. These patterns suggest the presence of various substituted aromatic compounds and PAHs in the carbon deposit, consistent with the incomplete combustion of both fossil and renewable fuels [46].

The FTIR results demonstrate that carbon deposit from biodiesel combustion contains more oxygenated functional groups compared to those from petroleum diesel and BHD. This reflects the higher inherent oxygen content of biodiesel relative to BHD (which lacks oxygen) and petroleum diesel, leading to biodiesel's greater tendency to form carboxylic acids, esters, and aromatic compounds during combustion. These molecular-level insights highlight the influence of fuel type on carbon deposit composition, which is critical for understanding engine deposits, emissions, and potential aftertreatment requirements.

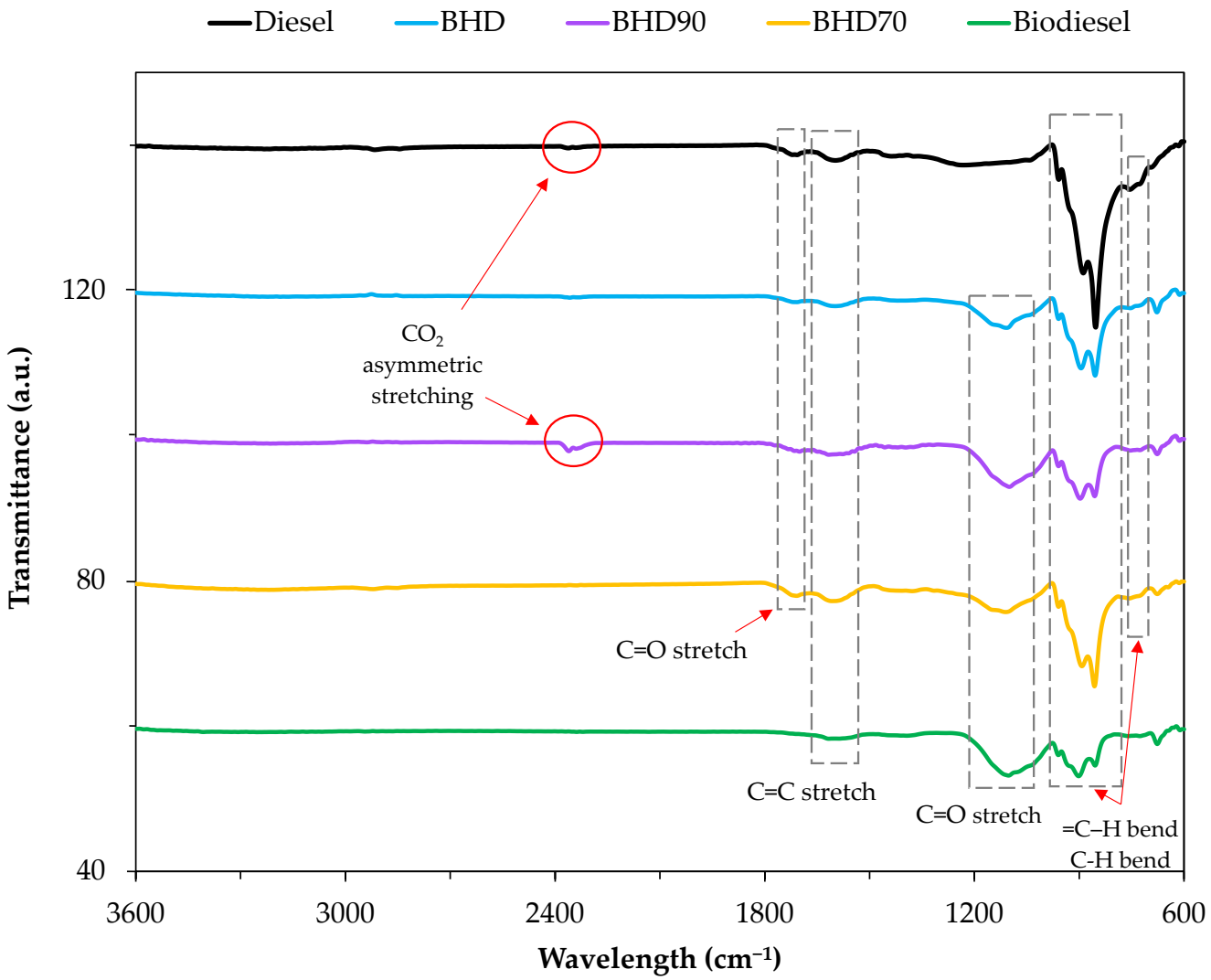


Figure 5. Infrared spectrum of accumulated carbon deposit on piston top from various fuels.

Table 14. Detected functional group of carbon deposit on piston top from various fuels.

Wavelength (cm^{-1})					Frequency of Wavelength (cm^{-1})	Vibration Type	Functional Group
Diesel	**BHD**	**BHD90**	**BHD70**	**Biodiesel**			
-	3187	3250	3200	-	3300–2500	O–H	carboxylic acid
2918, 2845	-	2919, 2852	-	-	3000–2850	C–H stretch	alkanes
2363	-	2361	-	-	2350–2360	CO_2 asymmetric stretching	CO_2
1709	1707	1709	1701	-	1710–1665	C=O stretch	unsaturated aldehydes, ketones
1597	1598	1609	1618	1586	1620–1450	C=C stretch	aromatic
-	-	1378	1397	1394	1440–1395	O–H bend	carboxyl
-	1108	1111	1100	1102	1320–1000	C–O stretch	alcohols, carboxylic acids, esters, ethers
-	959, 678	959, 676	959, 677	960, 902	1000–650	=C–H bend	alkenes
889, 854	895, 855	892, 856	897, 856	-	900–675	C–H bend	1,2,4-trisubstituted
755	753	758	754	-	770–730	C–H bend	monosubstituted benzene derivative

4. Conclusions

The growing adoption of bio-hydrogenated diesel (BHD) as a renewable alternative has raised concerns regarding its inadequate lubricity and potential engine wear under prolonged use. To address this issue, the tribological performance of BHD–biodiesel blends was evaluated under realistic engine operating conditions for 200 h. BHD90 emerged as the optimal fuel blend, providing superior engine protection with a torque reduction of only 11.2% and a fine iron particle concentration of 101 ppm, remaining well within safety limits. The addition of 10% biodiesel effectively enhanced lubricity to offset BHD's limitations while maintaining oxidation stability. In contrast, pure BHD demonstrated the most severe wear patterns among the BHD-based fuels, exhibiting a fine iron particle concentration of 273 ppm (36.4% above safety limits) and a 14.8% torque reduction. This study revealed a critical threshold where biodiesel content exceeding 10% became counterproductive due to accelerated oxidative degradation. Although BHD70 and pure biodiesel showed improved inherent lubricity, their oxidation levels reached 28.0 and 31.5 absorption units, respectively, indicating instability. These findings confirm that biodiesel's hygroscopic nature promotes oxidation, which counteracts its lubricity benefits at higher blending ratios. Additionally, FTIR analysis indicated that carbon deposits from biodiesel combustion contained higher levels of oxygenated compounds, whereas deposits from pure BHD and diesel primarily consisted of aliphatic hydrocarbons. Overall, BHD90 represents the optimal balance between renewable fuel content, engine protection, and operational durability, offering essential insights into future commercial fuel specifications and sustainable diesel applications.

Supplementary Materials: The following supporting information can be downloaded at: https://www.mdpi.com/article/10.3390/lubricants14040178/s1, Figure S1: GC chromatogram of diesel; Figure S2: GC chromatogram of BHD; Figure S3: GC chromatogram of biodiesel. Detailed chemical compositions derived from these chromatograms are reported in previous works [13,14].

Author Contributions: S.C.: Writing—original draft, Formal analysis, Conceptualization. A.M.: Writing—review and editing, Project administration, Conceptualization. N.K.: Visualization, Methodology, Investigation, Data curation. A.P.: Writing—original draft, Visualization, Investigation, Formal analysis. T.S.: Writing—review and editing, Visualization. E.S.: Writing—review and editing, Project administration, Formal analysis, Conceptualization. All authors have read and agreed to the published version of the manuscript.

Funding: This research was funded by the Program Management Unit for Competitiveness (PMUC), grant no. C10F640103.

Data Availability Statement: The data that support the findings of this study are available from the corresponding author upon reasonable request.

Acknowledgments: The authors would like to gratefully acknowledge the financial support provided by the Office of National Higher Education Science Research and Innovation Policy Council; Thailand Science Research and Innovation; the Program Management Unit for Competitiveness (PMUC); PTT Exploration and Production Public Co., Ltd.; Cherdchai Corporation Co., Ltd.; Polawat Engine Co., Ltd.; and Verasuwan Co., Ltd.

Conflicts of Interest: The authors declare that they have no known competing financial interests or personal relationships that could have appeared to influence the work reported in this paper.

Abbreviations

ATR-FTIR	Attenuated Total Reflectance Fourier-Transform Infrared Spectroscopy
BHD	Bio-Hydrogenated Diesel
FAMEs	Fatty Acid Methyl Esters

FTIR	Fourier-Transform Infrared Spectroscopy
GC	Gas Chromatography
GC-MS	Gas Chromatography–Mass Spectrometry
HFRR	High-Frequency Reciprocating Rig
ICP-AES	Inductively Coupled Plasma–Atomic Emission Spectrometry
PAHs	Polycyclic Aromatic Hydrocarbons
PQ Index	Particle Quantifier Index
RFS-AES	Rotrode Filter Spectroscopy–Atomic Emission Spectrometry
SAW	Surface Acoustic Wave
TBN	Total Base Number
TIS	Thai Industrial Standard

References

1. Kaewchada, A.; Akkarawatkhoosith, N.; Bunpim, D.; Bangjang, T.; Ngamcharussrivichai, C.; Jaree, A. Production of bio-hydrogenated diesel from palm oil using Rh/HZSM-5 in a continuous mini fixed-bed reactor. *Chem. Eng. Process.-Process Intensif.* **2021**, *168*, 108586. [CrossRef]
2. Fathurrahman, N.A.; Auzani, A.S.; Zaelani, R.; Anggarani, R.; Aisyah, L.; Maymuchar; Wibowo, C.S. Lubricity properties of palm oil biodiesel blends with petroleum diesel and hydrogenated vegetable oil. *Lubricants* **2023**, *11*, 176. [CrossRef]
3. Kuszewski, H.; Jaworski, A.; Szpica, D. Comparative Study of the Lubricity of Hydrotreated Vegetable Oil, Diesel, and Their Blends Using Four-Ball Testing: Focus on Scuffing Load. *Energies* **2025**, *18*, 3141. [CrossRef]
4. Lu, X.; Zhao, J.; Markov, V.; Wu, T. Study on precise fuel injection under multiple injections of high pressure common rail system based on deep learning. *Energy* **2024**, *307*, 132784. [CrossRef]
5. Filon, D.; Anastopoulos, G.; Karonis, D. Synthesis and Evaluation of Sunflower-Oil-Based Esters as Biolubricant Base Oils Using Ca/TEA Alkoxide Catalyst. *Lubricants* **2025**, *13*, 345. [CrossRef]
6. Firmansyah, R.A.; Perry Burhan, R.; Zetra, Y.; Prasetyoko, D. The development of triglyceride-based additives and their lubricity properties for low sulfur fossil diesel: A review. *J. Tribol.* **2022**, *144*, 100801. [CrossRef]
7. *ASTM D975-23*; Standard Specification for Diesel Fuel. ASTM International: West Conshohocken, PA, USA, 2023.
8. Chuepeng, S.; Klinkaew, N.; Thumanu, K.; Theinnoi, K.; Sukjit, E.; Dearn, K. Effects of castor oil as lubricity enhancer on friction and wear characteristics of piston engine running on diesohol. *Int. J. Engine Res.* **2025**, *26*, 1305–1318. [CrossRef]
9. Wang, E.; Liu, D.; Wang, S. Texture optimizing method for rotating shaft with lip seal considering processing errors. *Chin. J. Mech. Eng.* **2025**, *in press*. [CrossRef]
10. Zheng, Y.; Li, F.; Zhang, H.; Wang, S.; Zhao, Z.; Wang, W.; Chen, R. Fishhook characteristics of biodiesel lubricity during autoxidation. *Fuel* **2023**, *331*, 125897. [CrossRef]
11. Sriprathum, S.; Maneedaeng, A.; Klinkaew, N.; Sukjit, E. Comprehensive analysis of properties of green diesel enhanced by fatty acid methyl esters. *RSC Adv.* **2023**, *13*, 31460–31469. [CrossRef]
12. *ISO 12156-1:2018*; Diesel Fuel—Assessment of Lubricity Using the High-Frequency Reciprocating Rig (HFRR)—Part 1: Test Method. ISO: Geneva, Switzerland, 2018.
13. Pumpuang, A.; Klinkaew, N.; Wathakit, K.; Sukhom, A.; Sukjit, E. The influence of plastic pyrolysis oil on fuel lubricity and diesel engine performance. *RSC Adv.* **2024**, *14*, 10070–10087. [CrossRef]
14. Klinkaew, N.; Wiangkham, A.; Ariyarit, A.; Aengchuan, P.; Pumpuang, A.; Sripratum, S.; Maneedaeng, A.; Srisertpol, J.; Sukjit, E. Strategic optimization of engine performance and emissions with bio-hydrogenated diesel and biodiesel: A RVEA-GRNNs framework. *Results Eng.* **2024**, *24*, 103072. [CrossRef]
15. *ASTM D445-23*; Standard Test Method for Kinematic Viscosity of Transparent and Opaque Liquids (and Calculation of Dynamic Viscosity). ASTM International: West Conshohocken, PA, USA, 2023.
16. *ASTM D1298-17*; Standard Test Method for Density, Relative Density, or API Gravity of Crude Petroleum and Liquid Petroleum Products by Hydrometer Method. ASTM International: West Conshohocken, PA, USA, 2017.
17. *ASTM D240-19*; Standard Test Method for Heat of Combustion of Liquid Hydrocarbon Fuels by Bomb Calorimeter. ASTM International: West Conshohocken, PA, USA, 2019.
18. *ASTM D86-23*; Standard Test Method for Distillation of Petroleum Products and Liquid Fuels at Atmospheric Pressure. ASTM International: West Conshohocken, PA, USA, 2023.
19. *ASTM D976-16*; Standard Test Method for Calculated Cetane Index of Distillate Fuels. ASTM International: West Conshohocken, PA, USA, 2016.

20. *ASTM D93-20*; Standard Test Methods for Flash Point by Pensky-Martens Closed Cup Tester. ASTM International: West Conshohocken, PA, USA, 2020.
21. Department of Energy Business Thailand. *Notification of the Department of Energy Business: Characteristics and Quality of Diesel Fuel, B.E. 2567*; Government Gazette: Bangkok, Thailand, 2024; Volume 141.
22. *TIS 2618-2557*; Single Suction Centrifugal Electric Pumps: Energy Efficiency Requirements. Thai Industrial Standards Institute: Bangkok, Thailand, 2014.
23. *ASTM D4739-17*; Standard Test Method for Base Number Determination by Potentiometric Titration. ASTM International: West Conshohocken, PA, USA, 2017.
24. *ASTM D7414-20*; Standard Practice for Condition Monitoring of In-Service Lubricants by Trend Analysis Using Fourier Transform Infrared (FT-IR) Spectrometry. ASTM International: West Conshohocken, PA, USA, 2020.
25. *ASTM D7624-17*; Standard Practice for Monitoring Diesel Engine Oils by Remaining Useful Life Analysis Using Infrared Spectroscopy. ASTM International: West Conshohocken, PA, USA, 2017.
26. *ASTM D7844-22*; Standard Test Method for Condition Monitoring of Soot in In-Service Lubricants by Trend Analysis Using Fourier Transform Infrared (FT-IR) Spectrometry. ASTM International: West Conshohocken, PA, USA, 2022.
27. Hsieh, P.Y.; Bruno, T.J. A perspective on the origin of lubricity in petroleum distillate motor fuels. *Fuel Process. Technol.* **2015**, *129*, 52–60. [CrossRef]
28. Knothe, G.; Steidley, K.R. Lubricity of components of biodiesel and petrodiesel. The origin of biodiesel lubricity. *Energy Fuels* **2005**, *19*, 1192–1200. [CrossRef]
29. Nicolas, L.R.; Barker, J.; Clark, J.; Langley, G.J.; Herniman, J.M. Screening and classification of hydrogenated vegetable oils using a combination of SFC-FID, SFC-MS and GCxGC-MS. *Analyst* **2025**, *150*, 3578–3586. [CrossRef] [PubMed]
30. d'Ambrosio, S.; Mancarella, A.; Manelli, A. Utilization of hydrotreated vegetable oil (HVO) in a Euro 6 dual-loop EGR diesel engine: Behavior as a drop-in fuel and potentialities along calibration parameter sweeps. *Energies* **2022**, *15*, 7202. [CrossRef]
31. Roman, C.; Delgado Canto, M.Á.; García-Pérez, M.; Fernández-Silva, S.D.; Li, K.; García-Morales, M. Wear and Friction Behavior of Cellulose Nanofibers-Based Biogreases. *Lubricants* **2025**, *13*, 423. [CrossRef]
32. Shepel, O.; Matijošius, J.; Rimkus, A.; Duda, K.; Mikulski, M. Research of parameters of a compression ignition engine using various fuel mixtures of hydrotreated vegetable oil (Hvo) and fatty acid esters (fae). *Energies* **2021**, *14*, 3077. [CrossRef]
33. Theinnoi, K.; Tsolakis, A.; Chuepeng, S.; York, A.P.; Cracknell, R.; Clark, R. Engine performance and emissions from the combustion of low-temperature Fischer? Tropsch synthetic diesel fuel and biodiesel rapeseed methyl ester blends. *Int. J. Veh. Des.* **2009**, *50*, 196–212. [CrossRef]
34. El-Adawy, M. Effects of diesel-biodiesel fuel blends doped with zinc oxide nanoparticles on performance and combustion attributes of a diesel engine. *Alex. Eng. J.* **2023**, *80*, 269–281. [CrossRef]
35. Ni, P.; Zhang, Z.; Xu, H.; Wang, X.; Xia, Q. Diffusion and hygroscopicity of particles from diesel and biodiesel combustion in an environmental chamber. *Energy Rep.* **2022**, *8*, 8271–8281. [CrossRef]
36. Gupta, J.G.; Agarwal, A.K. Engine durability and lubricating oil tribology study of a biodiesel fuelled common rail direct injection medium-duty transportation diesel engine. *Wear* **2021**, *486*, 204104. [CrossRef]
37. Arthus, L.; Estevam, B.R.; Aguila, Z.J.; Maciel, M.R.W.; Fregolente, L.V. Facile tuning of hydrogel properties for efficient water removal from biodiesel: An assessment of alkaline hydrolysis and drying techniques. *Chem. Eng. Sci.* **2023**, *282*, 119224. [CrossRef]
38. Cican, G.; Mitrache, A. Numerical Simulation of Paraffin Energetic Performance Enhanced by KNO_3, NH_4NO_3, Al, Ti, and Stearic Acid for Hybrid Rocket Applications. *Fuels* **2025**, *6*, 54. [CrossRef]
39. Sabapathy, S.P.; Ammasi, A.M.; Khalife, E.; Babu, M.; Munusamy, S.; Sabapathy, P.; Gharehghani, A.; Szymanek, M.; Kaveh, M. Optimization of injection timing and ethyl hexyl nitrate additive effects on diesel engine characteristics using rubber seed oil biodiesel. *Int. J. Energy Res.* **2025**, *2025*, 1686933. [CrossRef]
40. Loo, D.L.; Teoh, Y.H.; How, H.G.; Teh, J.S.; Andrei, L.C.; Starčević, S.; Sher, F. Applications characteristics of different biodiesel blends in modern vehicles engines: A review. *Sustainability* **2021**, *13*, 9677. [CrossRef]
41. Zhao, E.; Zhang, G.; Li, Q.; Zhu, S. Impact of High-Concentration Biofuels on Cylinder Lubricating Oil Performance in Low-Speed Two-Stroke Marine Diesel Engines. *J. Mar. Sci. Eng.* **2025**, *13*, 1189. [CrossRef]
42. Agarwal, A.K.; Agarwal, D. Field-Testing of biodiesel (B100) and diesel-fueled vehicles: Part 2—Lubricating oil condition monitoring. *J. Energy Resour. Technol.* **2021**, *143*, 042308. [CrossRef]
43. Hao, L.; Du, B.; Gong, L.; Lou, T.; Lou, W. Molecular dynamics study of the effect of oxidation aging of FAMEs on biodiesel properties. *J. Mol. Liq.* **2023**, *392*, 123518. [CrossRef]
44. García, A.; Pastor, J.V.; Monsalve-Serrano, J.; Iñiguez, E. Detailed assessment of exhaust emissions in a diesel engine running with low-carbon fuels via FTIR spectroscopy. *Fuel* **2024**, *357*, 129707. [CrossRef]

45. Guo, J.; Li, F.; Zhang, H.; Duan, Y.; Wang, S.; Tan, F.; Chen, Y.; Lu, F.; Luo, L. Effects of fuel components and combustion parameters on the formation mechanism and emission characteristics of aldehydes from biodiesel combustion. *Renew. Energy* **2023**, *219*, 119474. [CrossRef]
46. Bukkarapu, K.R.; Krishnasamy, A. Fourier-transform-infrared-spectroscopy-based approach to predict engine fuel properties of biodiesel. *Energy Fuels* **2021**, *35*, 7993–8005. [CrossRef]

Disclaimer/Publisher's Note: The statements, opinions and data contained in all publications are solely those of the individual author(s) and contributor(s) and not of MDPI and/or the editor(s). MDPI and/or the editor(s) disclaim responsibility for any injury to people or property resulting from any ideas, methods, instructions or products referred to in the content.